

When hot meets cold: post-flare coronal rain

Wenzhi Ruan (✉ wenzhi.uan@kuleuven.be)

Centre for Mathematical Plasma Astrophysics

Yuhao Zhou

Centre for Mathematical Plasma Astrophysics, KU Leuven

Rony Keppens

Centre for Mathematical Plasma Astrophysics, KU Leuven <https://orcid.org/0000-0003-3544-2733>

Article

Keywords: Solar Flares, Post-flare Loops, Extreme Ultraviolet Passbands, Corona-chromosphere Mass and Energy Cycle, Reconnection-driven Flares, Multi-thermal Structuring

Posted Date: June 29th, 2021

DOI: <https://doi.org/10.21203/rs.3.rs-608655/v1>

License:  This work is licensed under a Creative Commons Attribution 4.0 International License.

[Read Full License](#)

When hot meets cold: post-flare coronal rain

Wenzhi Ruan ^{*1}, Yuhao Zhou¹, and Rony Keppens¹

¹Centre for mathematical Plasma Astrophysics, Department of Mathematics, KU
Leuven, Celestijnenlaan 200B, B-3001 Leuven, Belgium

June 22, 2021

All solar flares demonstrate a prolonged, hourlong post-flare (or gradual) phase, characterized by arcade-like, post-flare loops (PFLs) visible in many extreme ultraviolet (EUV) passbands. These coronal loops are filled with hot – ~ 30 MK – and dense plasma, evaporated from the chromosphere during the impulsive phase of the flare, and they very gradually recover to normal coronal density and temperature conditions. During this gradual cooling down to ~ 1 MK regimes, much cooler – ~ 0.01 MK – and denser coronal rain is frequently observed inside PFLs. Understanding PFL dynamics in this long-duration, gradual phase is crucial to the entire corona-chromosphere mass and energy cycle. Here we report the first simulation in which a solar flare evolves from pre-flare, over impulsive phase all the way into its gradual phase, which successfully reproduces post-flare coronal rain. This rain results from catastrophic cooling caused by thermal instability, and we analyse the entire mass and energy budget evolution driving this sudden condensation phenomenon. We find that the runaway cooling and rain formation also induces the appearance of dark post-flare loop systems, as observed in EUV channels. We confirm and augment earlier observational findings, suggesting that thermal conduction and radiative losses alternately dominate the cooling of PFLs. Since reconnection-driven flares occur in many astrophysical settings (stellar flares, accretion disks, galactic winds and jets), our study suggests a new and natural pathway to introduce multi-thermal structuring.

Solar flares represent explosive phenomena in the solar atmosphere, where $10^{28} - 10^{32}$ ergs of energy originally stored in the solar magnetic field can suddenly be released via magnetic reconnection [1, 2]. Reconnection is also considered to be relevant for many other types of flaring behaviours observed throughout the universe [3, 4]. The time development

*wenzhi.ruan@kuleuven.be

31 of a solar flare event can be divided into three phases: a preflare phase, a sudden, impulsive
32 phase and a gradual or post-flare phase [5]. The magnetic energy is released rapidly in
33 the impulsive phase within a typical timescale of (tens of) minutes. A large fraction of
34 this released energy is transported from the tenuous and hot corona downwards to the
35 denser and colder solar chromosphere via thermal conduction and by energetic electrons
36 [6, 7]. This deposition of energy in the chromosphere leads to a sudden heating of the
37 local plasma, and causes upward evaporation of the plasma to form super hot (~ 10 MK)
38 and dense ($\sim 10^{10} \text{ cm}^{-3}$) arcade-like loop systems at coronal heights. The loops return
39 to their usual coronal conditions (~ 1 MK, $\sim 10^8 - 10^9 \text{ cm}^{-3}$) in the following, gradual
40 phase, where field-guided thermal conduction and radiative losses generally contribute to
41 the cooling process [8, 9]. These loops, visible in extreme ultraviolet (EUV), but also in
42 $\text{H}\alpha$ images, are usually called post-flare loops (PFLs) [10].

43 Thanks to dramatically increased spatio-temporal resolutions in observations, this grad-
44 ual phase of solar flares is now known to show PFLs which spontaneously develop fine-scale
45 coronal rain [11, 12, 13, 14]. In the multi-thermal coronal rain events, cool and dense rain
46 blobs form in-situ in hot corona, to fall to the chromosphere with speeds up to 100 km s^{-1} .
47 Coronal rain is also observed in non-flaring coronal loops, is frequently found in loops of
48 active regions [15, 16, 17, 18, 19, 20, 21], and this type of coronal rain has been studied
49 previously using magnetohydrodynamic (MHD) simulations [22, 23, 24, 25, 26]. It has been
50 generally accepted that these rain blobs are generated in a catastrophic cooling process,
51 essentially caused by thermal instability [27, 28, 29, 30]. In a catastrophic cooling event,
52 local temperatures drop from 1 MK to below 0.1 MK within one minute, while local den-
53 sities can increase by orders of magnitude [14]. Observations of flare-driven coronal rain
54 demonstrate that this catastrophic cooling can also happen in PFLs, but this has thus
55 far never been modeled. The actual post-flare coronal rain trigger is yet to be identified:
56 recent work showed that it can not be due to electron beams [31]. Another phenomenon
57 thought to have a close relationship with these sudden condensations are the so-called dark
58 post-flare loops (DPFLs), where some PFL loops suddenly vanish from specific EUV pass-
59 bands, e.g. at 17.1 nm, 30.4 nm and 21.1 nm [32, 33, 34]. In these DPFLs, an EUV loop
60 which was bright for a while suddenly darkens for several minutes, so effectively disappears
61 between the adjacent EUV loops seen at the same height. It has been suggested that the
62 formation of cool and dense coronal rain may contribute to EUV emission and absorption,
63 inducing DPFL formation [33, 34]. However, this suggestion must still be confirmed in an
64 ab-initio model. Besides coronal rains, multi-thermal plasma behaviour is at stake in many
65 setting, e.g. in galactic outflows or in giant molecular clouds in the interstellar medium
66 [35, 36, 37].

67 Here we perform an MHD simulation of a flare event from its pre-flare phase all the
68 way into the gradual phase. This simulation finally allows us to understand the complex
69 thermodynamic evolutions of PFLs. For the first time in any modeling effort, we (1)
70 reproduce post-flare coronal rain; (2) quantify the chromosphere-corona mass and energy
71 cycles during PFLs; and (3) demonstrate the intricate relationship between condensations

72 and the disappearing EUV loops, or DPFLs.

73 Post-flare loop formation and evolution

74 In solar flare events, arcade-like PFLs form in the impulsive phase due to magnetic recon-
 75 nection and are filled with hot and dense plasma by evaporation flows from the chromo-
 76 sphere. In our two and a half dimensional (2.5D) simulation, we simulate the cross-sectional
 77 view on an extended flaring arcade system, with the assumption that plasma parameters
 78 do not vary in the direction across the arcade. The simulation plane runs perpendicular to
 79 the (evolving) flare ribbons that mark the PFL footpoints. The hot PFL plasma releases
 80 soft X-ray (SXR) photons via thermal bremsstrahlung and EUV photons of specific ener-
 81 gies due to electron de-excitation, making the PFLs light up in the SXR waveband and
 82 at selected EUV wavelengths. Synthesizing our MHD simulation in this early impulsive
 83 phase gives mock observational views shown in Fig. 1. Solar flares are classified as A, B,
 84 C, M or X level, according to their peak SXR flux in the 1-8 Å waveband measured near
 85 Earth. This peak flux in our simulation is about $4 \times 10^{-7} \text{ W cm}^{-2}$ when assuming that the
 86 loop width in the third direction is 100 Mm (see also Fig. 2e), therefore the simulated flare
 87 is a B level flare.

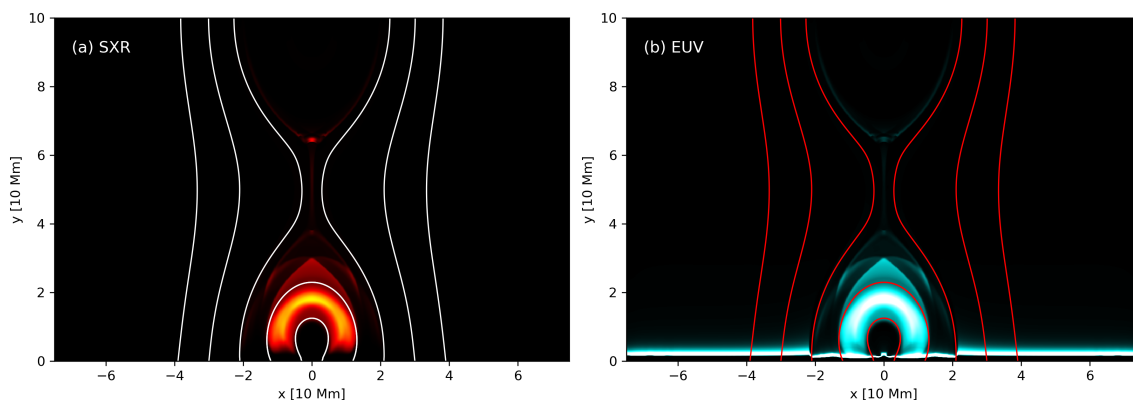


Figure 1: SXR (panel a, emission in 3-6 keV) and EUV image (panel b, at 13.1 nm) of our simulated flare at its impulsive phase ($t = 6$ min). The right, 13.1 nm emission has peak temperatures at $10^{5.6}$ K and 10^7 K. Solid lines are magnetic field lines.

88 Fig. 2 demonstrates the full evolution in magnetic topology, from pre-flare current sheet
 89 to the formation of PFLs at the impulsive phase (Fig. 2b), extended to the entire evolution
 90 of the PFLs through the gradual phase (Fig. 2c,d). There is a vertical current sheet
 91 separating regions of opposite field directions at the beginning of our simulation (Fig. 2a).

92 Magnetic reconnection inside this current sheet produces closed magnetic arcades below and
 93 a flux rope above a reconnection site in the impulsive phase ($t \lesssim 8$ min). A large amount of
 94 magnetic energy released by reconnection is conducted to the high density chromosphere
 95 and this produces upward evaporation flows. They fill the generated coronal loops with
 96 hot plasma (~ 10 MK) and increase the plasma number density by one order in the PFLs
 97 (Fig. 2b). Thereafter, the flare enters the gradual phase when we have a rapidly decreasing
 98 magnetic reconnection speed ($t \gtrsim 8$ min). The PFL temperature decreases slowly due
 99 to thermal conduction and radiative losses in this gradual phase, but suddenly triggers
 100 thermal instability near $t \simeq 35$ min. The loop density also decreases in this period, but is
 101 still much higher than the external coronal density (Fig. 2c).

102 Catastrophic cooling driven by thermal instability condenses local plasma in-situ and
 103 leads to high density (close to 10^{11} cm^{-3}) and cold (close to 0.01 MK) structures in the
 104 coronal PFLs (Fig. 2d). Fig. 2e shows how the SXR flux reaches its peak value at the
 105 impulsive phase, to then gradually decrease as the loop temperature drops. The temporal
 106 evolution of the total coronal rain material (i.e. $T_e < 0.1$ MK, $N_e > 10^{10}$ cm^{-3} and $y > 5$
 107 Mm) is also illustrated in Fig. 2e. We note that sudden condensations happen in two
 108 successive events during the entire simulated period. These are located in different loop
 109 systems, with the second rain event appearing at a higher altitude.

110 Once condensations happen within PFLs, the formed cold and dense plasma structures
 111 will likely fall down from coronal heights due to gravity and hence appear as observed
 112 coronal rain blobs. This is fully reproduced in our simulation as demonstrated in Fig. 3.
 113 Cold plasma is formed at a PFL looptop at the beginning of the runaway condensation
 114 (Fig. 3a). Thereafter, the cold structure extends to lower and higher loops, meanwhile
 115 sliding down to one side (Fig. 3b,c). This falling cold plasma gets accelerated to a speed
 116 of ~ 100 km s^{-1} by gravity before it enters the chromosphere (Fig. 3d-f). Such a speed
 117 is close to that found in coronal rain observations. Considering an acceleration timescale
 118 of 10 minutes, the average acceleration rate is lower than the acceleration of gravity. A
 119 detailed analysis of rain blob acceleration process for non-flaring (or quiescent) coronal rain
 120 was given in [22].

121 Mass and energy cycles during the gradual phase

122 Here we investigate the mass and energy cycles in our entire 100-minute simulation of the
 123 gradual phase and the role of condensations in it. To do so, we track mass and energy
 124 budgets into the coronal part ($y > 5$ Mm) of a loop section in which the first round of
 125 condensation happens. This loop section is always bounded by (a) the evolving magnetic
 126 field line with a fixed footpoint at $x = -25$ Mm at our lower $y = 0$ boundary; and by (b)
 127 a similarly evolving field line with footpoint at $x = -15$ Mm (Fig. 4a). As seen in Fig. 3
 128 and Fig. 4a, this region gets emptied during the first round of condensations, as matter
 129 collects along the field lines into localized rain blobs. This entire loop system continuously

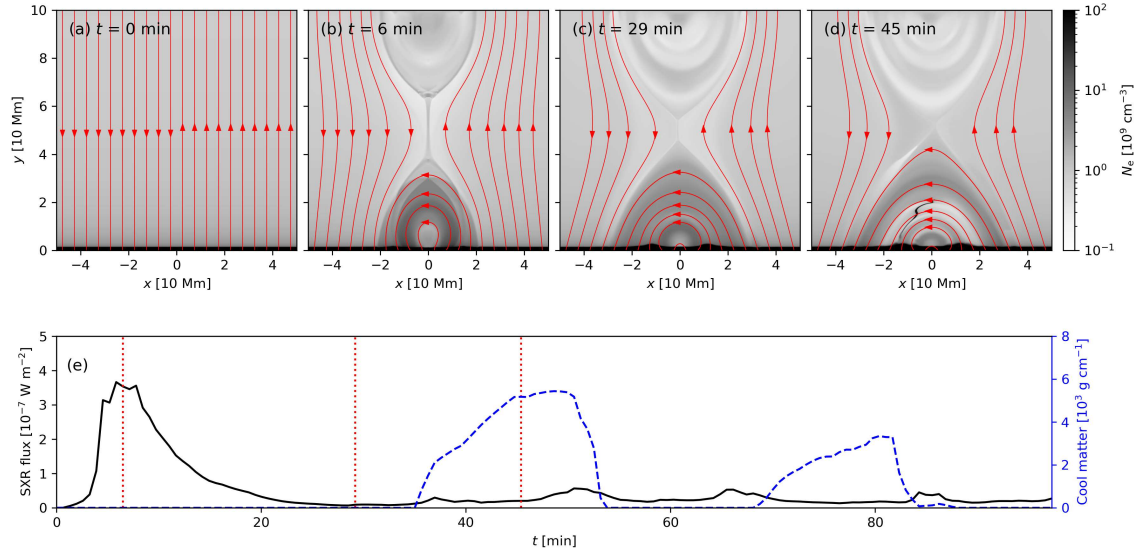


Figure 2: (a-d): Plasma number density (background color map) and magnetic field topology (in red) at $t = 0, 6, 29$ and 45 min. (e): Temporal evolution of the integral SXR flux (black solid line) and of the total coronal rain matter (blue dashed line). The PFLs have an assumed width of 100 Mm in the invariable z -direction, to calculate the SXR flux. The times corresponding to the top panels are indicated in panel (e) with vertical dotted red lines.

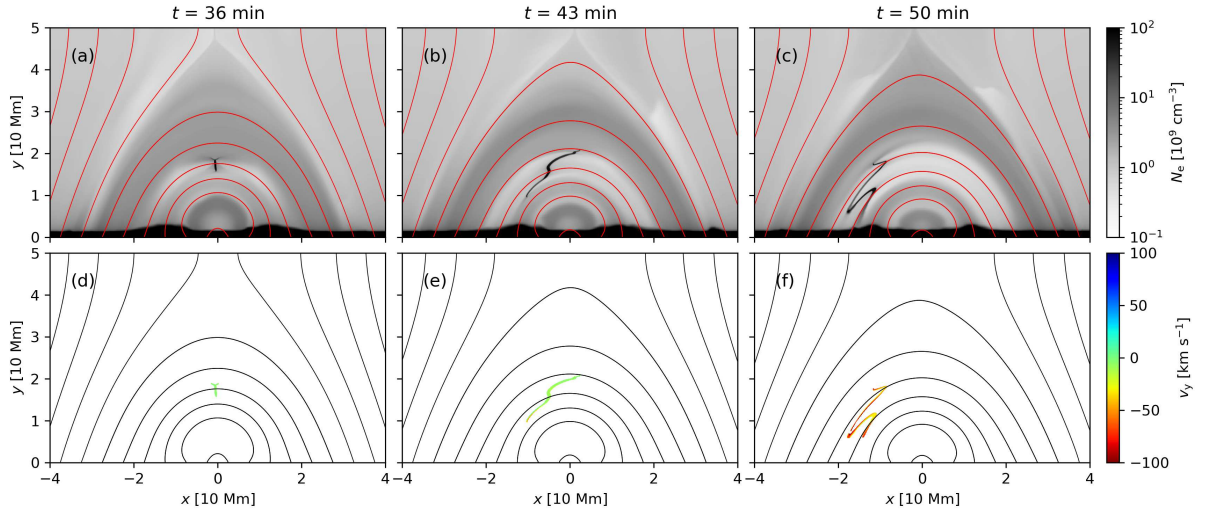


Figure 3: (a-c): Plasma number density at $t = 36, 43$ and 50 min. (d-f): Vertical y -component of velocity for the coronal cool plasma ($T_e < 0.1$ MK, $N_e > 10^{10}$ cm $^{-3}$ and $y > 5$ Mm). The solid lines are magnetic field lines.

130 moves downward as a result of the above reconnection dynamics and the corresponding
 131 area of the selected region continuously decreases during the simulation as quantified by
 132 the solid line in Fig. 4b. The area-integrated total energy (kinetic, thermal and magnetic
 133 combined, dashed line in Fig. 4b), area-integrated mass (solid line in Fig. 4c) and the
 134 area-averaged temperature (solid line in Fig. 4d) of this region also continuously decrease
 135 before the first condensation ($t \simeq 35$ min). Plasma which evaporated upwards into the
 136 corona in the previous impulsive phase now leaks back to the chromosphere in this period,
 137 seen in the downward mass flux (dashed line) in Fig. 4c. The decrease of temperature
 138 leads to a decrease of the atmospheric scale height. However, this downwards leakage of
 139 coronal plasma is severely reduced when the condensation happens after $t \gtrsim 35$ min, since
 140 the gas pressure in the coronal part of the loop then decreases rapidly. Therefore, we see
 141 a drop of the downward mass flux in Fig. 4c near $t \approx 38$ min, when condensations fully
 142 formed. Later on, the downward mass flux experiences a sudden increase, exactly when
 143 the cool coronal rain material goes through the lower $y = 5$ Mm boundary of the studied
 144 region. The area-integrated mass reaches its minimum value when all cool material leaves
 145 and enters the chromosphere. Thereafter, plasma from the chromosphere is injected to the
 146 loop again, due to the low pressure inside the loop, leading to an upwards mass flux. The
 147 total mass then gradually returns to its value before condensation.

148 The changing coronal energy budget shows a similar tendency with the changing coronal
 149 mass cycle. The energy also experiences a decrease in the pre-condensation and during the

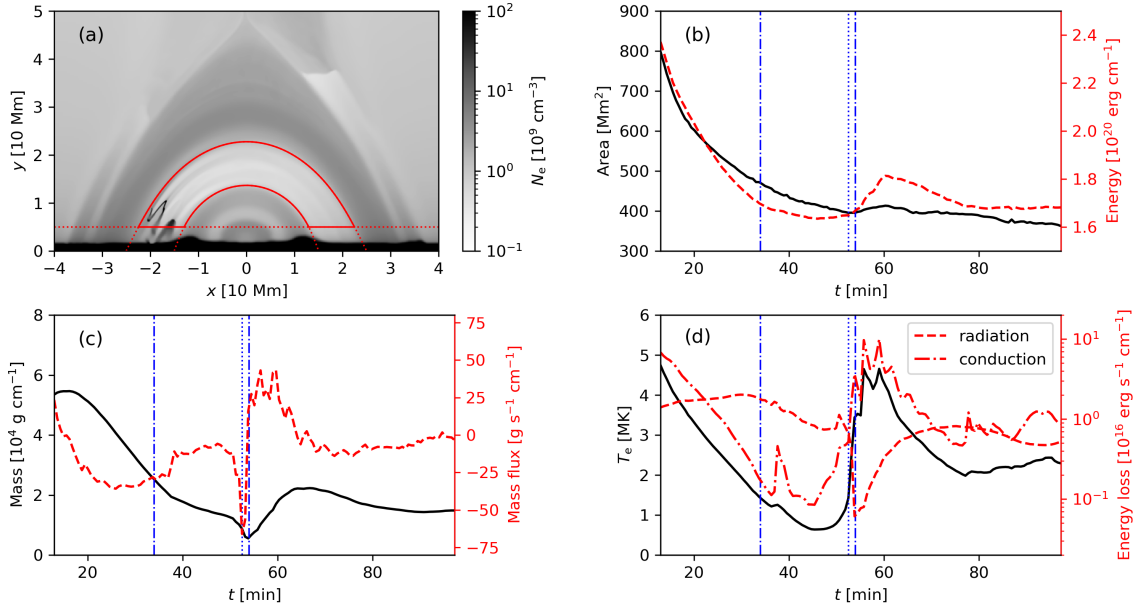


Figure 4: (a): Plasma number density at $t = 52$ min. The region bounded by the field lines starting from $(x, y) = (-25 \text{ Mm}, 0)$ and $(x, y) = (-15 \text{ Mm}, 0)$ and the horizontal line $y = 5 \text{ Mm}$ is investigated in panels b-d. (b): Time evolution of the evolving area (black solid line) and that of integrated total energy (red dashed line). (c): Time evolution of integrated mass (black solid line) and of the mass flux across the lower boundaries of this region. (d): Time evolution of average temperature (black solid line), integral radiative losses (red dashed line) and integral conductive losses (red dashed-dotted line). Blue vertical dashed-dotted lines indicate the starting and ending time of the condensation, and the vertical blue dotted line marks the time of panel a.

150 condensation phase, to then experience an increase after the condensations merged into
 151 the chromosphere due to renewed plasma injection (Fig. 4b). It has been suggested that
 152 thermal conduction determines the PFLs energy loss at the beginning of the gradual phase
 153 of a flare and that subsequently radiative losses will become dominant [38]. Our simulation
 154 shows that this suggestion is correct before and also during the occurring condensations.
 155 The efficiencies of radiative cooling and of thermal conduction to the energy loss in the
 156 selected region are compared in Fig. 4d. The contribution of thermal conduction is greater
 157 than radiative losses for $t \lesssim 25$ min, but conductive losses drop gradually owing to the
 158 decreasing temperature gradient. At $t \approx 25$ min, the average temperature is about 3 MK,
 159 and the efficiency of radiative losses becomes most prominent. However, conductive losses
 160 become stronger than radiative losses again when the condensations vanished from the
 161 loop system, as collisions between re-injected flows from both footpoints make the loop hot
 162 again and the radiative loss drop for a while due to the decrease of loop density.

163 Catastrophic cooling and rain-induced QPP

164 The first round of condensation happens near $t \approx 35$ min. The temporal evolutions of in-
 165 stantaneous maximum/minimum temperature/number density in the condensation region
 166 (the same as marked in Fig. 4a) are illustrated in Fig. 5. Triggering of thermal instability
 167 switches the radiative cooling process from linear to nonlinear, and then leads to a catas-
 168 trophic cooling of local plasma. We get an average temperature decreasing rate of -9000
 169 K s^{-1} in the catastrophic cooling phase. In contrast, the cooling rate before catastrophic
 170 cooling is -3000 K s^{-1} . As a result of catastrophic cooling, the local temperature decreases
 171 from 0.2 MK to 0.02 MK within half a minute (Fig. 5a), while the local number density
 172 increases by one order, from 10^{10} cm^{-3} to 10^{11} cm^{-3} (Fig. 5b).

173 A quasi-periodic pulsation (QPP) with a period of ~ 3 minutes appears in the maximum
 174 density curve, just after the rain condensation disappeared from the PFL system. This QPP
 175 is caused by the injected flows mentioned in the previous section, refilling and reheating
 176 the PFL. The density variation due to these flows along a field line is shown in Fig. 4c.
 177 Injected flows propagating from one footpoint to the other produce reflected slow mode
 178 waves. Such a process has previously been studied in [39] for isolated loop systems. The
 179 sharp density changes in Fig. 4c are shocks ahead of the injection flows and the wave fronts
 180 of the slow mode waves. Such QPPs hence reflect density variations in the low corona due
 181 to flows or wave propagation. The period of our QPP is close to the time for the slow
 182 mode wave to propagate from one footpoint to the other, as the wave speed is about 300
 183 km s^{-1} .

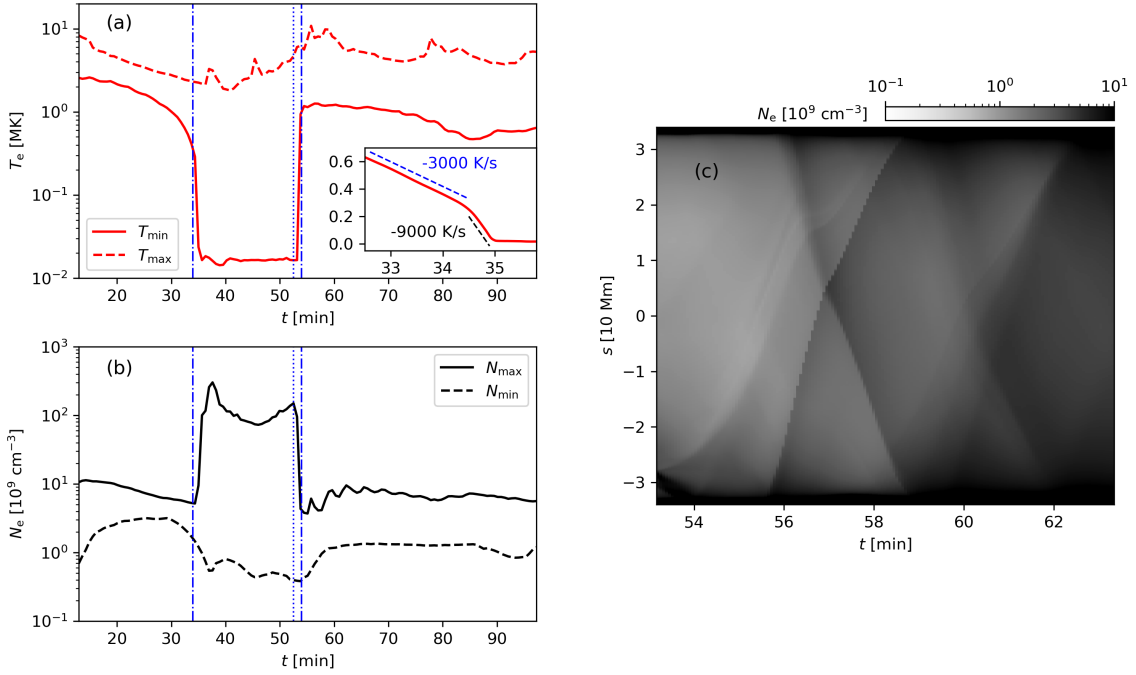


Figure 5: (a): Time evolution of maximum/minimum temperature in the region showing coronal rain from Fig. 4a. (b): Evolution of maximum/minimum number density in the same region. (c): Time-space plot of the number density along a field line with $y = 0$ footpoints at $x = \pm 24.5$ Mm, after the rain left the studied loop region, and a quasi-periodic oscillation appears. The midpoint of the field lines is at $s = 0$ and negative s indicates the left side.

184 Coronal rain and dark post-flare loops

185 In synthesized EUV images of our simulation, coronal loop(s) appear in the gradual phase.
 186 An example is shown in Fig. 6 at the 17.1 nm waveband. Interestingly, this loop disappears
 187 for about 10 minutes during the evolution, as demonstrated in panels (a) to (e) of Fig. 6.
 188 The sudden darkening of the bright EUV loop in our simulation resembles the dark post-
 189 flare loop (DPFL) phenomenon, previously observed at the same 17.1 nm passband and
 190 with similar timescale of 10 minutes [32]. Observed DPFLs and the disappearing EUV
 191 coronal loop in our simulation also share the same time evolution of integral EUV flux:
 192 the EUV flux reaches its minimum value when the darkening happens (compare Fig. 3 in
 193 ref. [32] and our Fig. 6f). The formation of a darkened coronal EUV loop needs to satisfy
 194 one or both of the following conditions: (1) an emission drop in an existing bright EUV
 195 loop; (2) an absorption of the background EUV emission [40]. Here we explain how these
 196 conditions can be satisfied based on our simulation results.

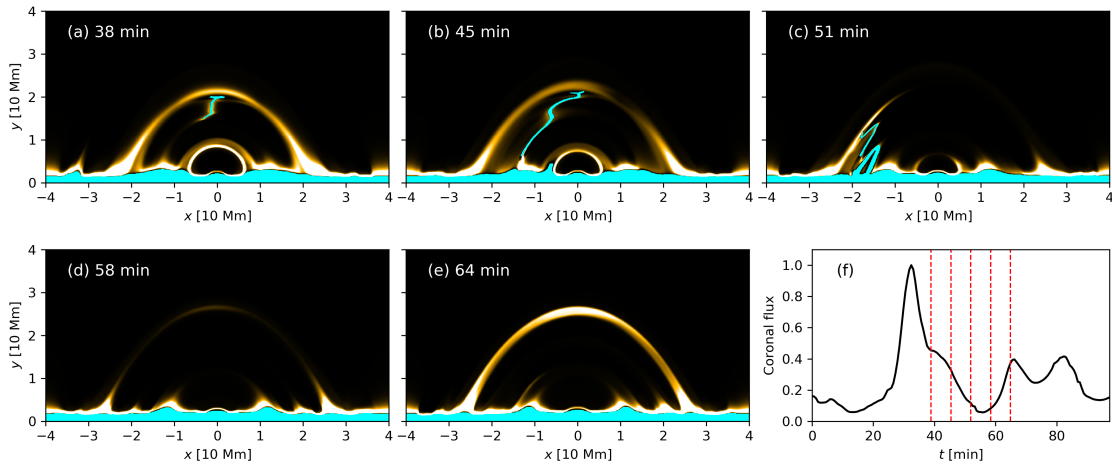


Figure 6: (a-e): Time evolution of synthetic EUV 17.1 nm images. The regions in cyan have temperatures lower than 0.1 MK. (f): Time evolution of the integral EUV 17.1 nm flux from a region $y > 5$ Mm. Red vertical dashed lines in panel (f) give the corresponding times of panels (a-e).

197 The role of cool and dense coronal plasma in EUV emission and absorption leading to
 198 DPFLs has been emphasized previously [33, 34], with coronal rain observations [11, 12, 13,
 199 14] and our simulation results showing how this cool and dense plasma can be generated in
 200 PFLs. The drop in the loop emission is understood from our simulation: loop temperature
 201 changes relate to nearby rain condensations. Indeed, the temperature of bright loops in
 202 this 17.1 passband (about $10^{5.8}$ K) is not far from the critical temperature for the onset

203 of catastrophic cooling (this is density and temperature dependent, but generally happens
204 below 2 MK according to [41]). Condensations can be triggered by thermal instability
205 near bright loops and these suddenly formed structures grow fastest across magnetic field
206 lines (counterintuitive due to the field-aligned thermal conduction, but see [22, 29, 30, 42]).
207 Rain that forms near (Fig. 6a-b), and ultimately inside (Fig. 6c) the bright coronal loops,
208 thus causes the darkening as illustrated in Fig. 6c-d. Once condensation happens, a lot
209 of plasma will collect into a small region, so the plasma density elsewhere in the loop
210 decreases. To maintain pressure balance, these evacuated loop regions will increase in
211 temperature, so EUV brightness decreases due to these combined temperature and density
212 changes. Ultimately, the loop refills and brightens once more (Fig. 6e).

213 **Summary**

214 To fully understand coronal rain in PFLs and the mass and energy budget in the gradual
215 phase of solar flares, we performed the first flare simulation from onset all the way into the
216 long duration post-flare phase. Post-flare coronal rain successfully and repeatedly forms.
217 The flare-induced rain is a result of catastrophic cooling by thermal instabilities, and our
218 simulation shows successive rain formation at increasing heights in the PFL configuration.
219 Falling rain blobs into the chromosphere lead to sudden mass drops in PFLs, but their
220 mass increases again due to spontaneously forming injection flows. Therefore, the coronal
221 rain events do not accelerate the PFL mass loss in the longer term. Such longer term mass
222 loss is more determined by the change of the gravity scale height due to the cooling of
223 PFLs.

224 Both thermal conduction and radiative losses contribute to the energy budget in PFLs.
225 Thermal conduction dominates the PFL energy loss at the beginning of the gradual phase.
226 Thereafter, it becomes less efficient than radiative losses, owing to decreases in loop tem-
227 perature and in temperature gradient. However, thermal conduction can efficiently recover
228 again after a condensation falls to the chromosphere, as the loop reaches again a high
229 temperature. In this phase, an emptied loop refills and can show a slow-wave related QPP.

230 We showed that the formation of DPFLs can result from post-flare rain condensations.
231 Condensations change loop temperatures and can make existing bright EUV loops tem-
232 porarily disappear for several minutes. This timescale of EUV loop darkening is identical
233 to observed DPFLs.

234 **Methods**

235 **Simulation setup**

236 We perform the simulation with the open-source MPI-AMRVAC code [43, 44]. The sim-
237 ulation is 2.5D, where the domain is 2D but all vector quantities have three components.

238 The simulation domain is given by $-75 \text{ Mm} \leq x \leq 75 \text{ Mm}$ and $0 \leq y \leq 100 \text{ Mm}$. This
 239 simulation box has an initial resolution of 96×64 , but an equivalent high resolution of
 240 3072×2048 is achieved with our block-adaptive mesh. The governing equations are the
 241 magnetohydrodynamic (MHD) equations with effects of gravity, thermal conduction, ra-
 242 diative loss and magnetic field dissipation due to resistivity included, also shown in [7]
 243 (the source terms related to fast electrons have not been activated here). The new multi-
 244 dimensional field-line-based transition region adaptive conduction (TRAC-L) method is
 245 adopted to properly handle the chromosphere-corona interaction at affordable resolution
 246 [45].

247 A relaxation has been done to obtain a static pre-flare atmosphere before we perform
 248 the flare simulation. A background heating is required to offset the energy losses due to
 249 radiative cooling and thermal conduction. Inspired by [46], this background heating is a
 250 function of initial and spatio-temporally evolving values, given by

$$H_b(x, y, t) = 0.5 \{ \tanh[(y - h_{tra})/h_a] + 1 \} N_{e,0}(y) N_e(x, y, t) \left(\frac{T_0(y)}{T(x, y, t)} \right)^2 G(T_0(y)), \quad (1)$$

251 where $h_{tra} = 3 \text{ Mm}$, $h_a = 0.1 \text{ Mm}$, N_e indicates number density, subscript 0 indicates the
 252 $t = 0$ initial value and $G(T)$ is the radiative cooling curve adopted in our simulations. The
 253 cooling curve from [47] is used. The initial vertical temperature $T_0(y)$ profile in [48] (model
 254 C7) is employed. The number density at $y = 40 \text{ Mm}$ is set to $2 \times 10^9 \text{ cm}^{-3}$ and the initial
 255 density profile is calculated based on hydrostatic equilibrium. In the relaxation stage, a
 256 uniform vertical magnetic field is adopted. A numerically static atmosphere is obtained
 257 after a relaxation time corresponding to 3.5 hours. The local number density at $y = 40$
 258 Mm decreases to about 10^9 cm^{-3} after this relaxation. The final instantaneous background
 259 heating rate of this relaxed stage is saved and then used in the subsequent flare simulation.

260 After the relaxation, the magnetic field configuration is changed. The magnetic config-
 261 uration from [46] is employed then, given by

$$B_x = 0, \quad (2)$$

$$B_y = \begin{cases} -B_0, & x < -\lambda \\ B_0, & x > \lambda \\ B_0 \sin[\pi x/(2\lambda)], & \text{else} \end{cases} \quad (3)$$

$$B_z = \sqrt{B_0^2 - B_y^2}, \quad (4)$$

262 where $B_0 = 30 \text{ G}$ is the new initial magnetic field strength and $\lambda = 10 \text{ Mm}$. Such
 263 a configuration allows magnetic reconnection. A three-stage resistivity strategy is then
 264 activated. A spatially localized resistivity inside the initial current sheet triggers magnetic
 265 reconnection in the first stage. This localized resistivity is given by

$$\eta(x, y, t < t_{\eta 1}) = \begin{cases} \eta_1 [2(r/r_\eta)^3 - 3(r/r_\eta)^2 + 1], & r \leq r_\eta \\ 0, & r > r_\eta \end{cases} \quad (5)$$

266 where $\eta_1 = 0.1$, $r = \sqrt{x^2 + (y - h_\eta)^2}$, $h_\eta = 40$ Mm, $r_\eta = 2.4$ Mm and $t_{\eta 1} = 31$ s. In the
 267 second stage, we use an anomalous resistivity given by

$$\eta(x, y, t_{\eta 1} < t < t_{\eta 2}) = \begin{cases} 0, & v_d \leq v_c \\ \min\{\alpha_\eta(v_d/v_c - 1) \exp[(y - h_\eta)^2/h_s^2], 1\}, & v_d > v_c \end{cases} \quad (6)$$

268 where $\alpha_\eta = 1 \times 10^{-3}$, $h_s = 10$ Mm, $t_{\eta 2} = 7.78$ min, $v_d(x, y, t) = J/(eN_e)$ and $v_c =$
 269 $128,000$ km s⁻¹. The resistivity is set to zero in the third stage $t > t_{\eta 2}$ to force the flare to
 270 enter the gradual phase, where only numerical dissipation happens. The resistivity strategy
 271 used in our first and second stage is similar to that in [49].

272 We employ symmetric boundary conditions for number density, pressure and magnetic
 273 field components, while anti-symmetric conditions are employed for velocity components at
 274 the left and right boundaries. At the upper and bottom boundaries, density and pressure
 275 are fixed to their initial values. The magnetic field components at the bottom boundary
 276 are also fixed to the initial values. An anti-symmetric condition is applied for the x -
 277 component of the magnetic field at our upper boundary, while the other two components of
 278 the magnetic field employ symmetric conditions there. The velocity at the upper boundary
 279 is set to zero. Anti-symmetric conditions are employed for the velocity components at the
 280 bottom boundary.

281 The SXR emission is calculated with the method reported in [50]. The EUV emissions
 282 are calculated with the contribution function provided by the CHIANTI database and the
 283 optically thin assumption [51].

284 Data Availability

285 Simulation data are available on request to W.Z.R. (wenzhi.uan@kuleuven.be).

286 Code availability

287 The simulation is performed with the open-source AMRVAC code [43, 44], which is available
 288 in website <http://amrvac.org>.

289 References

- 290 [1] P. A. Sweet, *Electromagnetic Phenomena in Cosmical Physics*, B. Lehnert, ed. (1958),
 291 vol. 6, p. 123.
- 292 [2] K. Shibata, T. Magara, *Living Reviews in Solar Physics* **8**, 6 (2011).
- 293 [3] B. Haisch, K. T. Strong, M. Rodono, *Ann. Rev. Astron. & Astrophys.* **29**, 275 (1991).
- 294 [4] E. M. de Gouveia Dal Pino, P. P. Piovezan, L. H. S. Kadowaki, *A&A* **518**, A5 (2010).

- 295 [5] S. R. Kane, *Coronal Disturbances*, G. A. Newkirk, ed. (1974), vol. 57, p. 105.
- 296 [6] S. K. Antiochos, P. A. Sturrock, *Astrophys. J.* **220**, 1137 (1978).
- 297 [7] W. Ruan, C. Xia, R. Keppens, *Astrophys. J.* **896**, 97 (2020).
- 298 [8] P. J. Cargill, J. T. Mariska, S. K. Antiochos, *Astrophys. J.* **439**, 1034 (1995).
- 299 [9] M. J. Aschwanden, D. Alexander, *Sol. Phys.* **204**, 91 (2001).
- 300 [10] A. Bruzek, *Astrophys. J.* **140**, 746 (1964).
- 301 [11] E. Scullion, L. Rouppe van der Voort, S. Wedemeyer, P. Antolin, *Astrophys. J.* **797**,
302 36 (2014).
- 303 [12] J.-C. Martínez Oliveros, *et al.*, *Astrophys. J. Lett.* **780**, L28 (2014).
- 304 [13] J. Jing, *et al.*, *Scientific Reports* **6**, 24319 (2016).
- 305 [14] E. Scullion, *et al.*, *Astrophys. J.* **833**, 184 (2016).
- 306 [15] J.-L. Leroy, *Sol. Phys.* **25**, 413 (1972).
- 307 [16] R. H. Levine, G. L. Withbroe, *Sol. Phys.* **51**, 83 (1977).
- 308 [17] C. J. Schrijver, *Sol. Phys.* **198**, 325 (2001).
- 309 [18] E. O'Shea, D. Banerjee, J. G. Doyle, *A&A* **475**, L25 (2007).
- 310 [19] P. Antolin, L. Rouppe van der Voort, *Astrophys. J.* **745**, 152 (2012).
- 311 [20] K. Ahn, *et al.*, *Sol. Phys.* **289**, 4117 (2014).
- 312 [21] P. Antolin, G. Vissers, T. M. D. Pereira, L. Rouppe van der Voort, E. Scullion,
313 *Astrophys. J.* **806**, 81 (2015).
- 314 [22] X. Fang, C. Xia, R. Keppens, *Astrophys. J. Lett.* **771**, L29 (2013).
- 315 [23] X. Fang, C. Xia, R. Keppens, T. Van Doorselaere, *Astrophys. J.* **807**, 142 (2015).
- 316 [24] S. P. Moschou, R. Keppens, C. Xia, X. Fang, *Advances in Space Research* **56**, 2738
317 (2015).
- 318 [25] C. Xia, R. Keppens, X. Fang, *A&A* **603**, A42 (2017).
- 319 [26] P. Kohutova, P. Antolin, A. Popovas, M. Szydlarski, V. H. Hansteen, *A&A* **639**, A20
320 (2020).
- 321 [27] E. N. Parker, *Astrophys. J.* **117**, 431 (1953).

- 322 [28] G. B. Field, *Astrophys. J.* **142**, 531 (1965).
- 323 [29] N. Claes, R. Keppens, *A&A* **624**, A96 (2019).
- 324 [30] N. Claes, R. Keppens, C. Xia, *A&A* **636**, A112 (2020).
- 325 [31] J. W. Reep, P. Antolin, S. J. Bradshaw, *Astrophys. J.* **890**, 100 (2020).
- 326 [32] Q. Song, J.-S. Wang, X. Feng, X. Zhang, *Astrophys. J.* **821**, 83 (2016).
- 327 [33] S. Ježič, L. Kleint, P. Heinzel, *Astrophys. J.* **867**, 134 (2018).
- 328 [34] P. Heinzel, *et al.*, *Astrophys. J. Lett.* **896**, L35 (2020).
- 329 [35] W. Banda-Barragán, *et al.*, *arXiv e-prints* p. arXiv:2011.05240 (2020).
- 330 [36] R. C. Dannen, D. Proga, T. Waters, S. Dyda, *Astrophys. J. Lett.* **893**, L34 (2020).
- 331 [37] M. M. Kupilas, C. J. Wareing, J. M. Pittard, S. A. E. G. Falle, *Mon. Not. R. Astron.*
332 *Soc.* **501**, 3137 (2021).
- 333 [38] P. J. Cargill, J. A. Klimchuk, *Astrophys. J.* **605**, 911 (2004).
- 334 [39] X. Fang, D. Yuan, T. Van Doorselaere, R. Keppens, C. Xia, *Astrophys. J.* **813**, 33
335 (2015).
- 336 [40] U. Anzer, P. Heinzel, *Astrophys. J.* **622**, 714 (2005).
- 337 [41] P. J. Cargill, S. J. Bradshaw, *Astrophys. J.* **772**, 40 (2013).
- 338 [42] Y. H. Zhou, P. F. Chen, J. Hong, C. Fang, *Nature Astronomy* **4**, 994 (2020).
- 339 [43] C. Xia, J. Teunissen, I. El Mellah, E. Chané, R. Keppens, *Astrophys. J. Suppl.* **234**,
340 30 (2018).
- 341 [44] R. Keppens, J. Teunissen, C. Xia, O. Porth, *Computers & Mathematics With Appli-*
342 *cations* **81**, 316 (2021).
- 343 [45] Y.-H. Zhou, W.-Z. Ruan, C. Xia, R. Keppens, *A&A* **648**, A29 (2021).
- 344 [46] J. Ye, *et al.*, *Astrophys. J.* **897**, 64 (2020).
- 345 [47] J. Colgan, *et al.*, *Astrophys. J.* **689**, 585 (2008).
- 346 [48] E. H. Avrett, R. Loeser, *Astrophys. J. Suppl.* **175**, 229 (2008).
- 347 [49] T. Yokoyama, K. Shibata, *Astrophys. J.* **549**, 1160 (2001).
- 348 [50] R. F. Pinto, N. Vilmer, A. S. Brun, *A&A* **576**, A37 (2015).
- 349 [51] G. Del Zanna, K. P. Dere, P. R. Young, E. Landi, H. E. Mason, *A&A* **582**, A56 (2015).

350 **Acknowledgements**

351 This work was supported by the ERC Advanced Grant PROMINENT, an FWO project
352 G0B4521N and a joint FWO-NSFC grant G0E9619N. This project has received funding
353 from the European Research Council (ERC) under the European Union’s Horizon 2020
354 research and innovation programme (grant agreement No. 833251 PROMINENT ERC-
355 ADG 2018). This research is further supported by Internal funds KU Leuven, through the
356 project C14/19/089 TRACESpace. The computational resources and services used in this
357 work were provided by the VSC (Flemish Supercomputer Center), funded by the Research
358 Foundation–Flanders (FWO) and the Flemish Government–department EWI.

359 **Author contributions**

360 W.Z.R performed the simulation and wrote the first draft. Y.H.Z contributed to the
361 implementation of the TRAC-L method and revision of the paper. R.K initiated the
362 study, supervised the project, led the discussions and contributed to revision of the paper.
363 All authors contributed to discussions.

364 **Competing interests**

365 The authors declare no competing interests.